

# Holographic Imaging of Crowded Fields: High Angular Resolution Imaging with Excellent Quality at Very Low Cost

R. Schödel<sup>1\*</sup>, S. Yelda<sup>2</sup>, A. Ghez<sup>2</sup>, J. H. Girard<sup>3</sup>, L. Labadie<sup>4</sup>,  
R. Rebolo<sup>5</sup>, A. Pérez-Garrido<sup>6</sup>, M.R. Morris<sup>2</sup>

<sup>1</sup>*Instituto de Astrofísica de Andalucía (CSIC), Glorieta de la Astronomía S/N, 18008 Granada, Spain*

<sup>2</sup>*Department of Physics and Astronomy, UCLA, Los Angeles, CA 90095-1547, USA*

<sup>3</sup>*European Southern Observatory (ESO), Casilla 19001, Vitacura, Santiago, Chile*

<sup>4</sup>*I. Physikalisches Institut, Universität zu Köln, Zùlpicher Str. 77, 50937 Köln, Germany*

<sup>5</sup>*Instituto de Astrofísica de Canarias, C/ Vía Láctea s/n, La Laguna, Tenerife E-38200, Spain*

<sup>6</sup>*Universidad Politécnica de Cartagena, Campus Muralla del Mar, Cartagena, E-30202, Spain*

## ABSTRACT

We present a method for speckle holography that is optimised for crowded fields. Its two key features are an iterative improvement of the instantaneous Point Spread Functions (PSFs) extracted from each speckle frame and the (optional) simultaneous use of multiple reference stars. In this way, high signal-to-noise and accuracy can be achieved on the PSF for each short exposure, which results in sensitive, high-Strehl reconstructed images. We have tested our method with different instruments, on a range of targets, and from the N[10  $\mu$ m]- to the I[0.9  $\mu$ m]-band. In terms of PSF cosmetics, stability and Strehl ratio, holographic imaging can be equal, and even superior, to the capabilities of currently available Adaptive Optics (AO) systems, particularly at short near-infrared to optical wavelengths. It outperforms lucky imaging because it makes use of the entire PSF and reduces the need for frame selection, thus leading to higher Strehl and improved sensitivity. Image reconstruction *a posteriori*, the possibility to use multiple reference stars and the fact that these reference stars can be rather faint means that holographic imaging offers a simple way to image large, dense stellar fields near the diffraction limit of large telescopes, similar to, but much less technologically demanding than, the capabilities of a multi-conjugate adaptive optics system. The method can be used with a large range of already existing imaging instruments and can also be combined with AO imaging when the corrected PSF is unstable.

**Key words:** instrumentation: high angular resolution, instrumentation: adaptive optics, atmospheric effects, methods: observational, techniques: high angular resolution, techniques: image processing

## 1 INTRODUCTION

Obtaining images at or near the diffraction limit of 4-10m class telescopes from the ground is key to many astrophysical projects. Before the end of the 1990s, this goal was generally reached by speckle interferometry, also called speckle imaging, a technique based on recording long series of short exposure images and digital image reconstruction *a posteriori* with a range of different algorithms (e.g., Labeyrie 1970; Knox 1976; Weigelt 1977; Lohmann et al. 1983; Christou et al. 1987; Christou 1991).

During the past two decades adaptive optics (AO) assisted observations have become the standard for obtaining near-infrared (NIR) images near the diffraction limit of large telescopes. An important advantage of AO is that the real-time image correction makes long integration times possible. This increases significantly the sensitivity of the observations, which is limited by the detector readout noise in speckle imaging, and also allows one to use techniques like coronagraphy or spectroscopy.

However, in spite of the enormous success of AO instrumentation, the technique is not perfect. A broad range of systematic effects can lead to difficulties in calibrating the AO PSF (see the ample discussion in Tuthill et al. 2006).

\* E-mail: rainer@iaa.es

**Table 1.** Summary of observations used in this work.

ID	Target	Instrument	UTC Date	$\lambda_c$ [ $\mu\text{m}$ ]	$DIT$ [s]	$N_{\text{Frames}}$	Seeing [ $''$ ]	Strehl
1	Galactic centre	NaCo/VLT	7 Aug 2011	2.18	0.15	12500	0.6 – 0.9	0.82
2	Galactic centre	NaCo/VLT	31 Mar 2009	2.18	1.0	1920	0.4 – 0.5	0.34
3	NGC 3603	NaCo/VLT	29 Jan 2010	1.27	0.11	4928	0.5	0.4
4	NGC 3603	NaCo/VLT	03 Aug 2010	2.18	0.4	4928	0.6	0.13
5	M15	FASTCAM/NOT	23 Oct 2008	0.872	0.03	50000	1.0	0.18
6	Galactic centre	VISIR/VLT	22/23 May 2007	8.59	0.02	$\sim 100000$	2.0 – 3.0	$> 0.9$
7	47 Tuc	NaCo/VLT	1 Aug 2010	2.18	3.0	1900	1.0	$> 0.9$
8	M 30	HAWKI/VLT	30 Apr 2012	2.15	0.2	128	0.9	

$\lambda_c$  is the central wavelength of the broad-band filter used.  $DIT$  (detector integration time) is the exposure time of individual frames.  $N$  is the total number of frames obtained. The *Strehl* column refers to the approximate Strehl ratio (uncertainty  $\sim 0.05$ ) reached in the optimal image reconstructed via our holography algorithm or in the final AO image (only for ID 2). The column titled *Seeing* lists the approximate visual seeing during the observations. No Strehl estimate is given for the observations of M 30 because the diffraction limit was strongly under-sampled in the observations (see section 4.10). Data sets ID 2 and ID 7 were obtained with, the rest without AO.

Another difficulty is that the PSF of an AO image varies systematically across the field-of-view (FOV) and that the Strehl ratio deteriorates rapidly with increasing distance from the guide star. These *anisoplanatic* effects result because different viewing directions probe different turbulence profiles of the atmosphere, but a single-conjugated AO system only corrects the wavefront toward the guide star.

Various solutions to these problems have been developed, like AO-assisted sparse aperture masking (SAM, Tuthill et al. 2006; Lacour et al. 2011) or multi-conjugate adaptive optics (e.g., Rigaut et al. 2000). In addition, the use of laser guide stars (LGSs) frees AO systems from the requirement of having bright stars close to the target. Nevertheless, all these solutions come at a price. Greater technical complexity is inevitably accompanied by rising costs and increased vulnerability of the systems. It is therefore important to keep exploring the possibilities of speckle imaging, which has, for example, recently experienced a renaissance at optical wavelengths, where AO still cannot work reliably, in the form of *lucky imaging* (see section 2).

In this paper we describe a new implementation of the so-called *speckle holography* technique. We have written a program package that provides excellent results based on iteratively improved extraction of the instantaneous PSF from speckle frames and on the optional simultaneous use of multiple reference stars. The algorithm has been specifically developed for crowded fields, but work also on isolated targets if at least one reference star is located sufficiently close. The algorithm shows excellent performance from the NIR to optical wavelengths, works with faint guide stars, and is more efficient than lucky imaging techniques. We tested our method on a broad range of targets, with different telescopes and instruments, and under various conditions. Table 1 summarizes the observations used in this work.<sup>1</sup> All data were reduced in a standard way (sky subtraction, dead pixel correction, flat-fielding).

<sup>1</sup> Based on observations made with ESO Telescopes at the La Silla Paranal Observatory under programmes 060.A-9800(J,L), 087.B-0658(A), 179.B-0261(X), and 485-L.0122(A).

## 2 SPECKLE IMAGE RECONSTRUCTION

A range of different algorithms exists for image reconstruction from speckle data. Among those, the so-called simple shift-and-add (SSA) method became one of the most widespread methods (e.g., Christou 1991; Eckart et al. 1994). In a simplified view, each speckle in the instantaneous PSF, or *speckle cloud* (see inset in top panel of Fig. 1), can be regarded as a diffraction-limited image of the source. The SSA method consists of applying a shift, given by the xy-offset of the brightest pixel of a reference star’s speckle cloud from a chosen reference pixel, to each sequential image in the stack before averaging the frames. The PSF in the resulting image can then be described by the superposition of an Airy function over a broad Gaussian seeing halo. With this method, typical Strehl ratios of the order 10% can be achieved at  $\lambda = 2.2 \mu\text{m}$  at an 8-m telescope.

The SSA algorithm became very popular because it is easy to understand, fast, and robust. On the downside, SSA makes inefficient use of the information and photons contained in the individual exposures. Thus the majority of the photons of a source end up in its seeing halo, which leads to low-Strehl, low-sensitivity images.

When combined with rigorous selection of the best frames, significantly higher Strehl ratios can be reached. This is due to the statistical nature of turbulence, which has the effect that a small percentage of the speckle frames will resemble diffraction limited short exposures, with little distortion by the atmosphere. This method is termed *lucky imaging* and has recently become popular at optical wavelengths (e.g. Hormuth et al. 2008; Labadie et al. 2010). While working well at small telescopes, lucky imaging becomes increasingly inefficient with larger telescope apertures because the mean number of speckles increases quadratically with telescope diameter. Thus, it can become necessary to discard 90–99% of the data in order to achieve a diffraction-limited image in the optical regime.

A more efficient image reconstruction algorithm is the so-called *speckle holography* technique. The algorithm is based on a division of averaged quantities in Fourier space:

$$O = \frac{\langle I_m P_m^* \rangle}{\langle |P_m^2| \rangle}, \quad (1)$$

where  $O$  is the Fourier transform of the object,  $I_m$  and  $P_m$

are the Fourier transforms of the  $m$ -th image (speckle frame) and of its instantaneous PSF, respectively, and the brackets denote the mean over  $N$  frames.  $P_m^*$  is the conjugate complex of  $P_m$ . Taking the average over a large number of frames will effectively suppress the noise.

It can be shown that equation 1 is the best estimate, in the least squares sense, of the Fourier transform of the object (Primot et al. 1990). For an infinite number of frames, the denominator becomes equal to the speckle transfer function related to the turbulence. This feature of the algorithm allows one to reconstruct a high-fidelity image from the combination of typically several hundreds to thousands of speckle frames. The actual image is then obtained after apodising  $O$  with the optical transfer function of the telescope (OTF, usually an Airy function) to suppress power above the telescope cut-off frequency and applying an inverse Fourier transform (see Petr et al. 1998, for a flow-diagram of the algorithm). The great advantage of speckle holography over the SSA technique is that it uses the *full* flux and information content of each speckle cloud. It thus results in significantly reduced seeing halos around point-sources and in higher Strehl ratios than the SSA technique. Frame selection is generally not necessary, which leads to a much higher observing efficiency ( $\sim 100\%$  of frames used) than in the case of lucky imaging ( $\sim 10\%$  of frames used, depending on seeing and telescope size). This increases significantly the sensitivity and dynamic range of the reconstructed images.

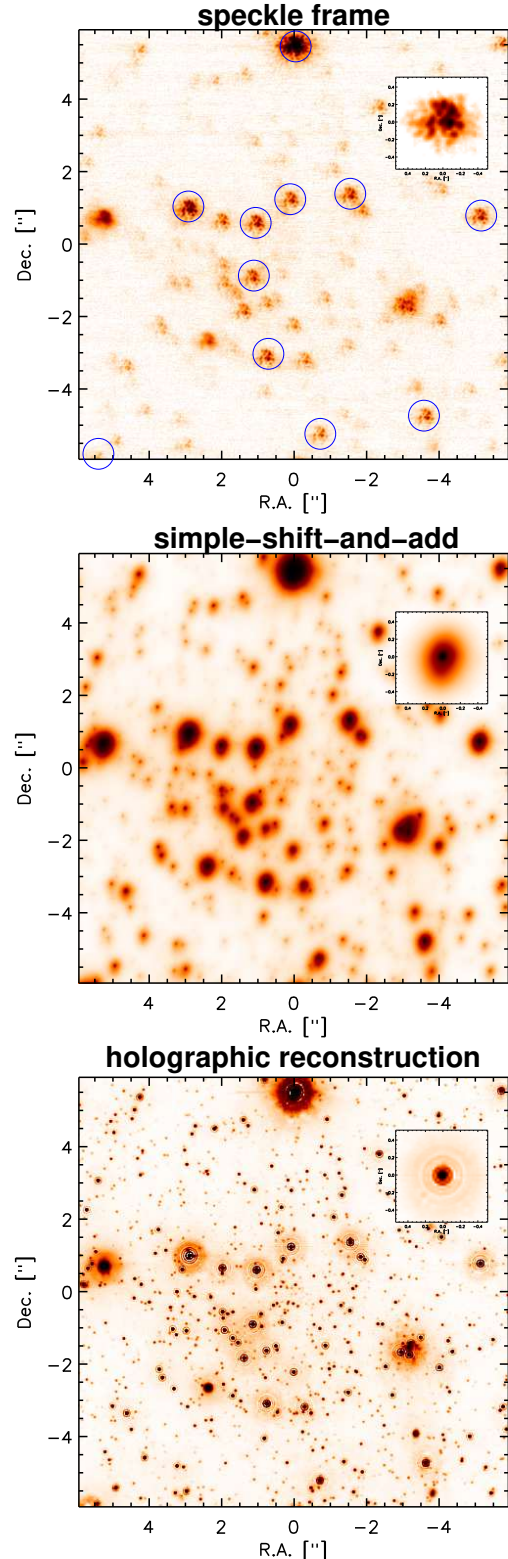
Key to a successful application of holography is the reliable extraction of the instantaneous PSF from each speckle frame. This poses no problem if a bright star is located close to the target, i.e. within an isoplanatic angle, and if this star is isolated, i.e. if there are no secondary sources present within the area covered by the speckle clouds. However, this ideal situation is rare. Secondary sources close to the reference star will lead to biases in the extracted instantaneous PSFs, which will result in systematic errors, such as the presence of positive or negative spurious sources (“ghosts”), in the reconstructed image. This poses an important obstacle to the use of speckle holography, particularly in crowded fields. Therefore, holography was in practice rarely used. Alternatively, *bispectrum*, or speckle masking, has been more commonly used because this technique allows one to reconstruct an image of complex targets without the necessity of observing an unresolved reference source (e.g., Weigelt 1977; Lohmann et al. 1983; Weigelt et al. 2006). But bispectrum methods are complex and require considerable amounts of computing time.

Here, we present an improved algorithm that addresses the key problem of speckle holography – the extraction of reliable instantaneous PSFs – in a twofold way: (a) the optional use of several reference stars *simultaneously*, which suppresses systematic errors caused by secondary sources near the reference stars, and (b) an *iterative* approach to PSF extraction, that uses the relative positions and fluxes of sources known from previous image reconstructions for the next iteration.

### 3 METHODOLOGY

Our method is illustrated using the example of the reduction of speckle data of the Galactic centre (GC, ID 1 in Table 1).

**Figure 1.**  $K$ s speckle observations of the Galactic centre. Top: Single speckle frame with reference stars used for reconstruction marked by circles (due to dithering one stars lies near the edge of the field shown here). Middle: SSA image. Bottom: Holographic reconstruction. Insets: PSFs for each image. All color scales are logarithmic.



The data were acquired with NaCo/VLT in the so-called *cube mode* (see Girard et al. 2010), that allows for the fast recording of a series of short exposures with a minimal overhead. Each cube comprised 500 frames. Visual seeing varied between  $\sim 0.6'' - 0.9''$  and the atmospheric coherence time was  $\tau_0 \approx 2$  ms, i.e. seeing was fast. We proceeded as follows:

- (i) Creation of long exposure images for each data cube.
- (ii) Pre-alignment of all cubes to remove dithering offsets.
- (iii) Image reconstruction with the SSA algorithm (middle panel of Fig. 1). Fine-alignment of the frames by using the centroids of the speckle clouds of the SSA reference star.
- (iv) Astrometry and photometry with *StarFinder* (Diolaiti et al. 2000) on the SSA-image. This provides relative positions (to sub-pixel accuracy) and fluxes of the stars which are needed to estimate (see vi) and iteratively improve the PSFs (see viii) for each frame.
- (v) Selection of reference stars (see top panel of Fig. 1).
- (vi) Estimation of the instantaneous PSF for each speckle frame from the median of the sub-pixel aligned, flux-normalized images of the reference stars.
- (vii) Noise thresholding: Estimation of noise,  $\sigma$ , and constant background,  $bg$ , for each PSF from its mean and standard deviation in a sufficiently large annulus around its centre. A constant value of  $bg + n \times \sigma$  (typically,  $n = 1 - 3$ ) is subtracted from the PSF. All pixels that acquire negative values through this subtraction are set to 0. Finally, a circular mask is applied to the PSF and it is normalized to a total flux of one.
- (viii) Subtraction of all known secondary, contaminating sources near the reference stars in each frame, using the preliminary PSFs and information from step (iv). Subsequently, improved PSF estimates are obtained for each frame (see inset in Fig. 1) by applying again steps (vi) and (vii).
- (ix)  $O$  is estimated by applying equation 1.
- (x) Apodization with the *OTF*. The *OTF* was assumed to be an Airy function, and was constructed with the routine *strehl* (ESO software package *eclipse*, Devillard 1997).
- (xi) Inverse Fourier transform to obtain the reconstructed image (bottom panel of Fig. 1).
- (xii) Repetition of the process, starting at step (iv) but using the holographically reconstructed image, which is of significantly higher quality than the initial SSA image. This means more stars are detected, with greater accuracy of their positions and fluxes. Reference stars that appear as close multiples or elongated in the holography image can be discarded. The result of this last iteration is shown in the bottom panel of Fig. 1.

Although the mean in equation 1 is very efficient in suppressing random noise, systematic errors can be present in the raw PSFs that are obtained from the median superposition of the reference stars. Sources of such systematic errors can be, e.g., the finite accuracy with which contaminating sources can be subtracted or features produced by the detector or readout electronics. Any additive offset to the PSF that may be caused by smooth, extended emission in the target must be taken into account. For these reasons it is important to apply the background subtraction and noise thresholding in step (vii). Mainly due to this noise thresholding, some of the flux in the reconstructed image ends up in halos around the stars. The noise thresholding would be

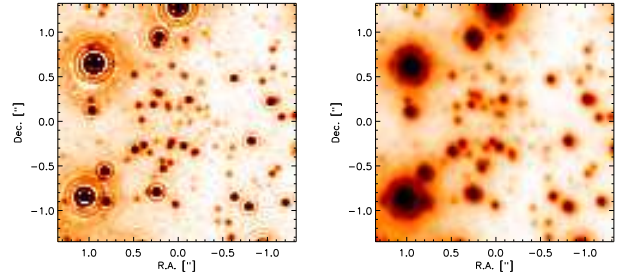


**Figure 2.** Zoom onto a  $\sim 2.5'' \times 2.5''$  region centred on Sgr A\* (NaCo/VLT,  $Ks$ ). Left: Image reconstructed from speckle data (ID 1 in Table 1) with our holography algorithm. Right: AO assisted image (ID 2 in Table 1). Note that some of the fast-moving stars near Sgr A\* are located at different positions in the two images, which were taken more than 2 years apart.

unnecessary if the reference star(s) were perfectly isolated and there were no sources of systematic uncertainties.

The SSA image (Fig. 1, centre) has an estimated Strehl ratio of  $\sim 9\%$ , while the holographic reconstruction (Fig. 1, bottom) leads to  $\sim 82 \pm 5\%$ . The Strehl and its uncertainty were estimated from three PSFs created with *StarFinder* using three different, non-overlapping sets of reference stars.

### 3.1 Quality control

Details of our astrometric and photometric examination of the image resulting from our holographic reconstruction method are given in appendix A. Here we only note that the image has an extremely high Strehl ratio and very good PSF cosmetics. Photometric uncertainties are  $\leq 1\%$  and astrometric uncertainties  $\leq 0.01$  pixel for stars having  $Ks \leq 15$ . Spatial and temporal PSF stability are high. Simulations show no systematic bias in the astrometry and photometry of point sources. Moreover, the noise properties of the image are largely Gaussian and no significant cross-correlations between the pixels could be detected.

### 3.2 Comparison with AO imaging

We compared the holographic image of the GC with a  $Ks$ -band AO image of the same region. The quality of the AO data chosen here (ID 2 in Table 1) is exceptionally high, with visual seeing of only  $0.4'' - 0.5''$  and an extremely long coherence time of  $\tau_0 \sim 47$  ms. The loop of the AO was closed on IRS7, the brightest star visible in the image shown in the panel (a) of Fig. 1. A comparison between the holographically reconstructed image from August 2011 and the AO image from March 2009 is shown in Fig. 2, which shows a zoom onto the region surrounding Sagittarius A\* (Sgr A\*).

A quantitative comparison of PSF fitting photometry in the AO and in the holography images is shown in Fig. 3. The analysis was done on a  $13'' \times 13''$  field centred on Sgr A\*. The detection threshold of *StarFinder* was set to  $5\sigma$  and the correlation threshold to 0.9 in order to suppress the detection of spurious sources. The *noise map* method, as described in appendix A was used to estimate the pixel uncertainties in both images. As can be seen in the left panel of Fig. 3, the AO image is about 1.5 mag deeper than the holography



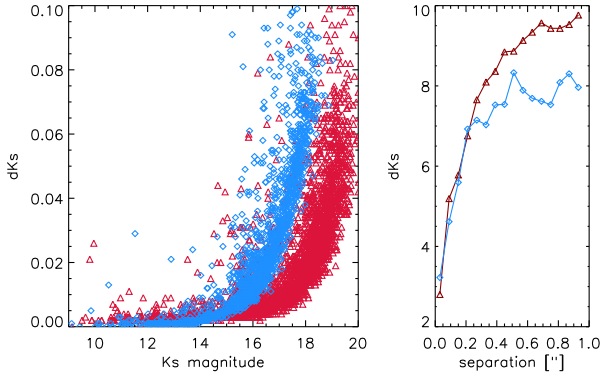


**Figure 3.** Photometry in the holographic (blue diamonds) and AO (red triangles)  $Ks$ -band images of the GC. Left: Photometric uncertainty vs. magnitude. Right: Dynamic range vs. separation for stellar pairs.

image. Note that this is hard to see in Fig. 3, which shows the most crowded region of the field, around Sgr A\*, where the completeness limit is  $Ks \sim 18$ . It is interesting to note that the photometric uncertainty for stars  $Ks \leq 14$  in the holography image is smaller than in the AO image. The right panel of Fig. 3 shows the dynamic range for the detection of close point sources in both images. The figure shows the median of the five stellar pairs with the highest dynamic range in each bin of  $0.06''$  width (one resolution element). At separations  $< 0.2''$ , the dynamic range of the holography image is equivalent to that of the AO image. We believe that the larger dynamic range of the AO image at separations  $> 0.2''$  is mainly caused by the higher sensitivity of the AO image, which contains a far greater number of faint stars.

For an exact quantitative comparison between holography and AO the data should be taken under the same atmospheric conditions with the same on-source integration times, of course. We note, however, that the comparison shown here is a conservative one, favouring the AO image, because seeing was significantly better for the AO observations. In particular, the coherence time was a factor  $> 10$  longer than for the speckle observations and unusually long for conditions at Paranal ( $\tau_0 \leq 6.6$  ms 95% of the time in the interval 1999-2003, as found on the ESO web site). We also note that the magnitude of the guide star, IRS 7, an irregular variable, was  $Ks = 6.96 \pm 0.04$  (measured after repairing its saturated core with *StarFinder*) during the AO observations,  $\sim 0.5$  mag brighter than at other times ( $Ks = 7.69 \pm 0.06$  in April 2006, Schödel et al. 2010), which will have resulted in improved AO performance compared to other epochs.

A further comparison between the performance of SSA, AO, and holographic imaging is shown in appendix B, where we describe the application of holographic imaging to NIRC/Keck GC imaging data. In fact, it was NIRC/Keck data on which we developed and fine-tuned large parts of our software.

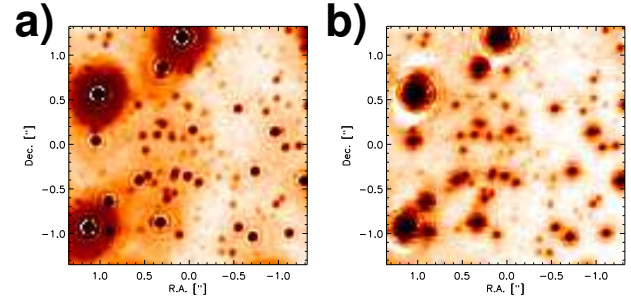


**Figure 4.** (a) Holographic reconstruction of the NaCo/VLT  $Ks$ -band GC speckle data with 24 reference stars of  $Ks \approx 13$ , distributed throughout the field, within about  $15''$  of Sgr A\*, which is located at the origin of this image. (b) Holographic reconstruction of the same image, but using only the bright supergiant IRS 7, located  $\sim 5.5''$  north of Sgr A\*.

## 4 HOLOGRAPHY UNDER EXTREME CONDITIONS

In this section we explore the limits of holographic imaging under different, extreme conditions, to demonstrate its great utility with a broad range of instruments and under a great variety of scenarios. We will also discuss questions such as the capability of holography to reconstruct extended targets or to deal with anisoplanatic effects.

### 4.1 Faint PSF reference stars

The faintest stars barely visible on the individual speckle frames taken on the GC have  $Ks \approx 13$ . We successfully tested image reconstruction by using a single, isolated star of  $Ks = 12$  and obtained an image with very good image cosmetics and a Strehl ratio of  $\sim 18\%$ . The limiting brightness for a natural guide star for NaCo's AO is heavily dependent on atmospheric conditions. It is roughly  $Ks \approx 12$ , leading to an estimated Strehl  $< 10\%$ . In a further test, by combining 24 reference stars of  $Ks = 13 \pm 0.5$ , distributed throughout the field, a Strehl  $\sim 45\%$  was reached (Fig. 4, left). This ability to work with (multiple) faint, NIR reference sources supersedes the possibilities of most, if not all, currently existing AO systems.

### 4.2 Centre of correction

Contrary to AO with a single, natural guide star, holographic imaging of a dense cluster allows the observer to choose the centre of optimal correction. As an illustration, we reconstructed the image using only the brightest star in the field, IRS 7, as reference source. Since IRS 7 is located approximately  $5.5''$  north of Sgr A\*, the correction is not optimal in the environment of the black hole (Fig. 4, panel (b)), in contrast to the images shown in Fig. 2, panel (a) or in Fig. 1, where the reference stars were chosen distributed throughout the field around Sgr A\*.

### 4.3 Extended sources

Reconstruction of extended sources presents no difficulties. This has been demonstrated by Schödel et al. (2011),

who created holographically reconstructed high-Strehl mid-infrared (MIR) images of the interstellar medium at the GC.

#### 4.4 Long exposure times

Since the short exposure times necessary for speckle imaging require windowing on some detectors (e.g.  $512 \times 512$  on the NaCo detector for  $DIT = 0.1$  s), a question of high interest is whether the speckle imaging technique can also work with exposure times significantly longer than an atmospheric coherence time. To test this, we observed NGC 3603, using  $DIT = 0.4$  s (ID 4 in Table 1), which allowed us to take advantage of the full NaCo detector FOV. The diffraction limit was reached with a Strehl of  $\sim 13\%$ . We conclude that diffraction-limited imaging is possible even with exposure times that exceed the atmospheric coherence time by factors  $\gg 10$  ( $\tau_0$  was a few ms during the observations), albeit at the cost of a lower Strehl in the final image.

#### 4.5 Short NIR and optical wavelengths

The reconstructed image from  $J$ -band speckle observations of the core of NGC 3603 (ID 3 in Table 1) is shown in the left panel of Fig. 5. With the three brightest stars (magnitudes  $J \approx 9$ ) used as reference sources, a Strehl of  $\sim 40\%$  was achieved. This supersedes the predicted performance of NaCo's AO. The *NaCo preparation software* (<http://www.eso.org/sci/observing/phase2/SMGuidelines/-NAOSPS.html>) can be used to get a rough idea of AO performance in the  $J$ -band. It predicts an on-axis Strehl ratio of about 20% under similar atmospheric conditions and with a *visual* guide star of  $V = 9$ . With an infrared guide star of  $J = 9$  the predicted on-axis Strehl is about 13%.

In order to test the performance of holography in the optical regime, we used  $I$ -band observations of the core of the globular cluster M15, obtained with FASTCAM (Labadie et al. 2010) at the 2.5-m Nordic Optical Telescope (NOT) (ID 5 in Table 1). After selecting the best  $\sim 1\%$  of the data, a Strehl of  $\sim 4\%$  and a dynamic range of about 5 magnitudes (assuming a  $5\sigma$  detection limit in *StarFinder*) were achieved with the *lucky imaging* technique. With holography the result on the same set of selected frames could be considerably improved, reaching a Strehl of  $\sim 27\%$  with a dynamic range of about 6.3 magnitudes. Selection of the speckle frames with the best PSFs is not necessary for holography. Therefore, by using the best 50% of the frames, we were able to increase the dynamic range of the holographic image even further, to about 8.0 magnitudes. Using an even larger amount of frames was not possible for the data used here because they were taken under very bad and highly variable seeing conditions, so that even the brightest stars were barely visible in many frames.

#### 4.6 Anisoplanatic effects

In the  $I$ -band, the isoplanatic angle is only on the order of a few arcseconds, while the FOV of FASTCAM is about  $15''$ . We divided the FOV into five overlapping subfields, each of size about  $9.5''$ . Holographic reconstruction was applied to these subfields separately, using several reference

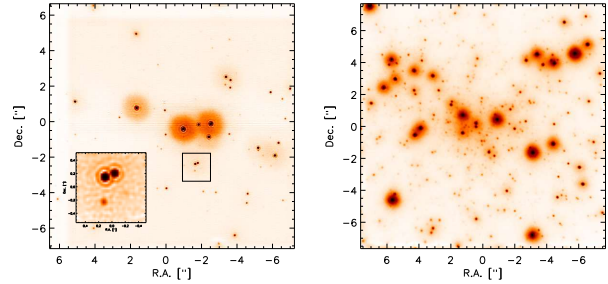


**Figure 5.** Left: Reconstructed  $J$ -band image of the core of NGC 3603. The inset shows a zoom of the region marked by the black box. The two close stars in the box are separated by  $0.078''$  and have  $J = 12.0$  and  $J = 12.6$ . Right: Reconstructed  $I$ -band image of the core of M15. Five overlapping subfields were reconstructed separately to counteract anisoplanatic effects.

stars in each one. The final image was created by mosaicking the reconstructed subfields together. The optimal shifts between them were determined via cross-correlation. The corresponding image has a highly homogeneous PSF across the field and is shown in the right panel of Fig. 5. About 10 stars with  $I = 12 - 13$ , distributed over the field, were used as reference sources for the holographic reconstruction.

#### 4.7 MIR wavelengths

Speckle techniques are naturally suited to improve images in the MIR because of the short readout times necessary at these wavelengths. In Schödel et al. (2011) we reconstruct fully diffraction limited ( $\text{FWHM} \approx 0.25''$ ), high-Strehl ( $\geq 90\%$ ) images of the Galactic centre from VISIR/VLT  $8.6 \mu\text{m}$  speckle imaging data during visual seeing as bad as  $\sim 2 - 3''$ . This shows that in the MIR, holography allows one to obtain high-Strehl images even under the most adverse seeing conditions. This can greatly enhance the flexibility and efficiency of such observations at large telescopes.

#### 4.8 Reference sources with extended emission

Holography can also work if the reference source is surrounded by diffuse emission. The reference star used for the MIR imaging described above, IRS3, sits atop extended, diffuse emission. In that case it is merely necessary to set the noise threshold in the PSF determination high enough to suppress the contribution of the diffuse emission (see Schödel et al. 2011, for more details). Increasing the noise threshold will make holography, which uses the entire PSFs, ever more similar to the *weighted shift-and-add* method, which uses only the relatively weighted local maxima of the instantaneous PSFs (Christou et al. 1987).

#### 4.9 Holography with AO

The necessarily short exposure time in speckle imaging limits the sensitivity to faint sources. Longer exposure times become possible with the help of AO. However, application of the holography technique will only be preferable if the AO PSF is *not completely* stable, i.e. if the PSF shows some

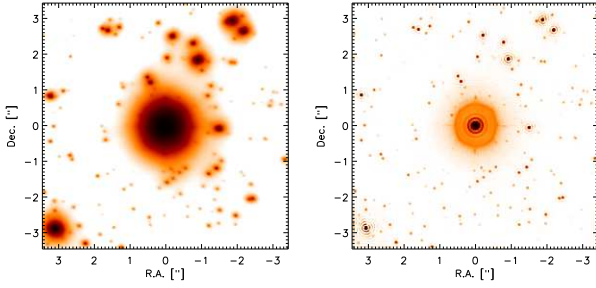


**Figure 6.** Left: AO-assisted  $K_s$ -band image of a field centred on the star 2MASS 00241142-7205556 in the globular cluster 47 Tuc. Right: Holographic image reconstruction of the same data.

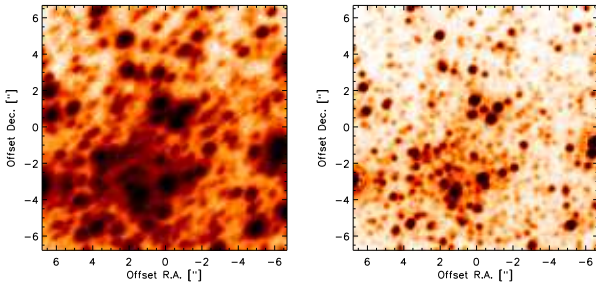


**Figure 7.**  $K_s$ -band imaging of M30 with VLT/HAWKI. Left: Standard long exposure with a resolution of  $\sim 0.7''$ . Right: Holographic reconstruction with a resolution of  $\sim 0.27''$ .

random variability on time scales similar to the exposure time. In that case, the holography technique can efficiently suppress the random fluctuations and lead to high-Strehl images.

We have tested this *holography plus AO* technique on imaging data of a field in the globular cluster 47 Tuc (ID 7 in Table 1). In these data the PSF is strongly variable between the frames. In Figure 6 we show a comparison between a standard reduction and a holographic image reconstruction of the same set of frames. The central star in the field was used as reference source. Application of holographic reconstruction improves the resolution of the image, without the strong ringing of Wiener deconvolution or the grainy background of Lucy-Richardson deconvolution. Hence, just as the performance of SAM can be boosted by the stabilizing effects of AO, so too can speckle holography. Holography can be very useful when AO correction is unstable, for example, under bad seeing conditions or at short wavelengths.

#### 4.10 Under-sampling: larger FOV and improved sensitivity

Using holography on imaging data that under-sample the diffraction limit can have two important advantages. First, each detector pixel will receive more photons, thus improving the sensitivity of speckle observations. Second, a much larger instrumental FOV can be achieved. The angular resolution that can in this case be reached is, of course, limited by the spatial frequency sampled adequately by the pixel

scale. But this can still be significantly better than the limit imposed by atmospheric seeing. We tested this idea with data acquired by the HAWKI NIR widefield camera installed at the ESO VLT on the globular cluster M30 (ID 8 in Table 1). An image of the cluster centre that results from simple, incoherent averaging of all exposures (corresponding to a standard long-exposure) is shown in the left panel of Figure 7. It has a PSF FWHM of roughly  $0.7''$ . Since the diffraction limit was under-sampled, we restored the holographic reconstruction with a Gaussian PSF of 2.5 pixel FWHM (corresponding to  $0.27''$  with the HAWKI pixel scale). The holographic reconstruction is shown in the right panel of Figure 7. The image sharpness was improved by more than a factor of two. Stars as faint as  $K_s \sim 20$  could be detected in spite of the short exposure time (0.2 s) and total integration time (26 s).

For technical reasons (non-optimal setup and very short observations, large dithering), we only show a small field in Fig. 7. Note, however, that with  $DIT = 0.2$  s the HAWKI detector can be read out in a  $512 \times 2048$  pixel field, corresponding to a FOV of  $217'' \times 54''$  or 3.25 square arc-minutes. Moreover, stars as faint as  $K_s \sim 16$  can be detected in the speckle frames and thus serve as reference for image reconstruction. Since holography can work with significantly longer exposure times (see section 4.4), even larger FOVs and fainter guide stars will be feasible.

It may be possible to even recover some of the information lost by under-sampling of the diffraction limit. When the condition of Nyquist sampling is not fulfilled, the detailed appearance of the speckle clouds of different stars in the field will depend significantly on the relative pixel positions of the stars. However, using a large number of exposures and multiple reference stars, one may recover some of the lost information, similar to dithering by half-pixels in observations with the Hubble Space Telescope's wide-field NIC3 camera (e.g. Wang et al. 2010). However, we have not yet tested this possibility.

## 5 SUMMARY AND DISCUSSION

An optimized method for applying holographic reconstruction to speckle imaging data of dense stellar fields has been presented. The two key features of our methodology are an iterative improvement of the instantaneous PSFs extracted from each speckle frame and the (optional) use of several reference stars simultaneously. The method has been tested with great success on a range of different instruments, wavelengths and targets. Excellent PSF cosmetics and high Strehl ratios have been achieved. The results show that holographic imaging can in many cases compete with AO imaging and even outperform it, particularly at short wavelengths. In the following, we briefly discuss the advantages and disadvantages of speckle holography in given observing situations, particularly with respect to alternatives, like AO-assisted imaging or SAM.

### 5.1 Sensitivity

The sensitivity in holographic imaging is usually limited by detector readout noise. Note that, to zeroth order, sensitivity is independent of the telescope diameter,  $D$ , because both

the number of photons collected and the number of pixels needed to sample the diffraction limit increase as  $D^2$ .

However, the constraints on sensitivity are not severe: In just 1900 s of total integration time, we have reached a  $3\sigma$  point-source sensitivity of  $Ks \approx 19$  in observations of the GC with the S27 camera of NaCo/VLT. The sensitivity of holographic imaging is clearly superior to the SSA/lucky imaging method. It is far more sensitive than SAM, even if the latter is supported by AO, because the masks block on the order of 90% of the light. The sensitivity of holography means that the technique can be well suited to study star clusters in the Milky Way. Main sequence stars of G-type can be detected out to 10 kpc; pre-main sequence stars at the H-burning limit with an age  $< 10^7$  yr can be detected out to  $\sim 3$  kpc.

Sensitivity can be improved by optimizing readout electronics for short exposure times. For example, the group of G. Weigelt (MPIfR, Bonn, Germany, priv. comm.) has reached a readout noise on the order of  $10e^-$  in their speckle camera, using a HAWAII-1 detector. NaCo uses the same detector type, but has a readout noise that is almost 4 times higher (in the fast readout modes required for speckle imaging), corresponding to a reduction of sensitivity of almost 1 magnitude. The next generation of fast, noiseless NIR detectors will provide a sensitivity on the order of 3 magnitudes deeper (e.g. Finger et al. 2010; Figer et al. 2011).

As we show in section 4.10, under-sampling of the diffraction limit is another, rather easy, way to improve sensitivity. Under-sampling the diffraction limit by a factor of  $\sim 3$  (corresponding to a resolution  $\sim 0.18''$  at an 8m-class or  $\sim 0.05''$  at a 30m-class telescope in the K-band) would increase sensitivity by more than one magnitude.

Finally, for a given sky brightness, the number of sky photons per pixel will depend on angular resolution. At small  $D$ , and therefore large pixel scale, infrared images will be sky-limited at far shorter readout times than with a large telescope. For example, with NOTCam at the 2.5 m NOT, noise is limited by the sky already for readout times  $\leq 0.5$  s, assuming a sky brightness of  $Ks = 13 \text{ mag arcsec}^{-2}$ . This means that the short readout times required by holography will not lead to any significant loss in sensitivity in the infrared at small telescopes.

## 5.2 Reference stars

Holography can achieve high Strehl ratios even with relatively faint ( $Ks \approx 13$ ) reference stars, particularly when multiple reference stars can be combined. No special infrared wavefront sensor is needed. Holography is thus naturally suited to peer into the most obscured places of the Galaxy (e.g., its central region) which may even be challenging for LGS observations because of a lack of tip-tilt stars.

## 5.3 Anisoplanatic effects

Image reconstruction *a posteriori* provides the great advantage that anisoplanatic effects can be compensated, as we have demonstrated in section 4.6. All that is needed is a sufficient density of reference stars in all parts of the field. The FOV is then, in principle, only limited by the detector size and the ability to read the latter with sufficient speed. In

the case of AO, such a feat would require extremely complex MCAO systems with multiple lasers (e.g., Neichel et al. 2010). Thus, holography is ideal for imaging large fields in Galactic targets such as young (and embedded) clusters, the bulge, the Galactic centre, or globular clusters. We believe that the method can be refined, for example by using interpolation or principal component decomposition to determine the instantaneous PSF at any location in the field. This is, however, beyond the scope of this work.

## 5.4 PSF calibration

Speckle holography results in a well-calibrated PSF with good cosmetics. A necessary condition is, however, the presence of either an isolated bright star near the science target or, alternatively, that the science target be embedded in a star cluster. For bright, isolated science targets, AO-assisted SAM is the preferable technique because it can guarantee a highly accurate PSF calibration using off-target calibration sources. Also, the dynamic range of AO assisted SAM for the detection of companion point sources around bright ( $Ks < 12$ ) stars can be as high as  $\Delta m \approx 6.5$  at separations  $\lambda/D$  (Lacour et al. 2011), where  $D$  is the telescope diameter and  $\lambda$  the observing wavelength. Hence, at the smallest angular scales and for bright targets ( $Ks \leq 10 - 12$  with NaCo, depending on AO correction) aperture masking surpasses the capabilities of holography demonstrated here.

Modern telescopes are highly adaptive and are conceived with many control loops (active optics, adaptive optics, etc.) which can limit the performance of techniques that require fast switching between science target and calibrator (e.g., SAM). For such techniques, it is very important that the telescope optical transfer function stay constant during the entire observation. This is rather difficult to guarantee with a VLT-like (thin mirror) telescope and will probably be nearly impossible with the next generation of extremely large telescopes. Because of the possibility of *self-calibration*, speckle holography may therefore remain an attractive technique even with the next generation of telescopes and AO systems.

## 5.5 Short wavelengths

Our experiments show that, at short wavelengths, holography out-competes most, if not all, currently existing AO systems as well as the lucky imaging approach. Since holography greatly reduces the need for frame selection, it can significantly boost the efficiency of optical speckle observations. Holography may currently represent the best approach for high angular resolution imaging at short NIR to optical wavelengths at telescopes of the 10m-class and even for the future extremely large telescopes.

## 5.6 Specialized techniques

Holography is a technique that is optimal for imaging, but is difficult to combine with additional techniques that require long integration times with a stable PSF, like spectroscopy or coronagraphy. Although it is possible to combine speckle imaging with spectroscopy (see, e.g., Genzel et al. 1997), use of an AO system appears clearly to be superior because of



the far greater sensitivity. Nevertheless, since a speckle camera can be built with a very small number of mirrors, holography appears to be a technique well suited for polarimetry.

AO-assisted SAM (see Tuthill et al. 2006) and holography can be highly complementary techniques. A good example is the science case of examining multiplicity in stellar clusters. Under optimal conditions SAM can provide a dynamic range of  $\sim 500$ , or about 6.7 magnitudes, at angular separations  $\theta = \lambda/D$ , where  $\lambda$  is the observing wavelength and  $D$  is the telescope diameter ( $\theta \approx 0.03''$  at the VLT in the  $K$ -band). However, aperture masking will only work on the brightest targets and on small fields. Holography can fill in data for larger fields and fainter stars, albeit at larger angular separations.

### 5.7 Speckle holography and AO

A very interesting perspective is to combine the virtues of both AO and holographic image reconstruction. Such an approach can be highly advantageous in situations where the AO system can only partially stabilize the PSF, for example when it operates at short wavelengths or under very unstable seeing conditions. We have provided a demonstration of the latter application in section 4.9. Of course, speckle holography can also be an extremely useful backup method when an AO system fails to close the loop or suffers temporary technical problems.

### 5.8 Costs and effectiveness

The greatest strengths of a speckle imaging system are arguably costs, robustness, and reliability. Only fast readout and data storage capabilities combined with a low-noise detector and electronics are necessary. No complex, expensive systems that require long development and debugging times are needed. The simplicity of a speckle system also means that it is highly reliable and will work under a broad range of circumstances. Additionally, a speckle camera will be of low weight and thus pose little strain upon any telescope infrastructure.

A particularly attractive option is that holographic imaging can be used with a large range of existing instruments, e.g.: VISIR, NaCo, and HAWK-I (VLT); FASTCAM (NOT); ASTRALUX (CAHA); ASTRALUX SUR (NTT), INGRID (WHT), NOTCAM (NOT, with the new readout electronics scheduled for the end of 2012), or NIRC2 (Keck). This is probably just a small subset of instruments having the necessary capabilities. We generally recommend short readout times be implemented on any optical or infrared imaging system that significantly over-samples the angular resolution set by atmospheric seeing.

### ACKNOWLEDGMENTS

RS acknowledges support by the Ramón y Cajal programme, by grants AYA2010-17631 and AYA2009-13036 of the Spanish Ministry of Economy and Competition, and by grant P08-TIC-4075 of the Junta de Andalucía. Support for this work was provided by NSF grant AST0909218 and the Levine-Leichtman Family Foundation. RS thanks Sridhar Rengaswamy for providing his speckle data simulation tool

and support in using it and Guillaume Montagnier and the ESO staff for taking the NACO and HAWK-I data presented in this work. Optical data are from observations made with the Nordic Optical Telescope in the Spanish Observatorio del Roque de los Muchachos. We thank the anonymous referee for reviewing this paper.

### REFERENCES

- Christou J. C., 1991, *Experimental Astronomy*, 2, 27
- Christou J. C., Freeman J. D., Hege E. K., 1987, in J. W. Goad ed., *Interferometric Imaging in Astronomy The Weighted Shift-and-Add Method*. p. 51
- Devillard N., 1997, *The Messenger*, 87, 19
- Diolaiti E., Bendinelli O., Bonaccini D., Close L. M., Currie D. G., Parmeggiani G., 2000, in P. L. Wizinowich ed., *Society of Photo-Optical Instrumentation Engineers (SPIE) Conference Series Vol. 4007 of Society of Photo-Optical Instrumentation Engineers (SPIE) Conference Series*, StarFinder: an IDL GUI-based code to analyze crowded fields with isoplanatic correcting PSF fitting. pp 879–888
- Eckart A., Genzel R., Hofmann R., Sams III B. J., Tacconi-Garman L. E., Cruzalebes P., 1994, in Genzel R., Harris A. I., eds, *NATO ASIC Proc. 445: The Nuclei of Normal Galaxies: Lessons from the Galactic Center Diffraction Limited Near-Infrared Imaging of the Galactic Center*. p. 305
- Figer D. F., Lee J., Hanold B. J., Aull B. F., Gregory J. A., Schuette D. R., 2011, in *Society of Photo-Optical Instrumentation Engineers (SPIE) Conference Series Vol. 8151 of Society of Photo-Optical Instrumentation Engineers (SPIE) Conference Series*, A photon-counting detector for exoplanet missions
- Finger G., Baker I., Dorn R., Eschbaumer S., Ives D., Mehrgan L., Meyer M., Stegmeier J., 2010, in *Society of Photo-Optical Instrumentation Engineers (SPIE) Conference Series Vol. 7742 of Society of Photo-Optical Instrumentation Engineers (SPIE) Conference Series*, Development of high-speed, low-noise NIR HgCdTe avalanche photodiode arrays for adaptive optics and interferometry
- Genzel R., Eckart A., Ott T., Eisenhauer F., 1997, *MNRAS*, 291, 219
- Ghez A. M., Salim S., Weinberg N. N., Lu J. R., Do T., Dunn J. K., Matthews K., Morris M. R., Yelda S., Becklin E. E., Kremenek T., Milosavljevic M., Naiman J., 2008, *ApJ*, 689, 1044
- Gillessen S., Eisenhauer F., Trippe S., Alexander T., Genzel R., Martins F., Ott T., 2009, *ApJ*, 692, 1075
- Girard J. H. V., Kasper M., Quanz S. P., Kenworthy M. A., Rengaswamy S., Schödel R., Gallenne A., Gillessen S., Huerta N., Kervella P., Kornweibel N., Lenzen R., Mérand A., Montagnier G., O’Neal J., Zins G., 2010, in *Society of Photo-Optical Instrumentation Engineers (SPIE) Conference Series Vol. 7736 of Society of Photo-Optical Instrumentation Engineers (SPIE) Conference Series*, Status and new operation modes of the versatile VLT/NaCo
- Hormuth F., Hippler S., Brandner W., Wagner K., Hennig T., 2008, in *Society of Photo-Optical Instrumentation Engineers (SPIE) Conference Series Vol. 7014 of Presented at the Society of Photo-Optical Instrumentation*

- Engineers (SPIE) Conference, AstraLux: the Calar Alto lucky imaging camera
- Knox K. T., 1976, *Journal of the Optical Society of America* (1917-1983), 66, 1236
- Labadie L., Rebolo R., Femenía B., Villó I., Díaz-Sánchez A., Oscoz A., López R., Pérez-Prieto J. A., Pérez-Garrido A., Hildebrandt S. R., Béjar-Sánchez V., José Piqueras J., Rodríguez L. F., 2010, in *Society of Photo-Optical Instrumentation Engineers (SPIE) Conference Series Vol. 7735 of Society of Photo-Optical Instrumentation Engineers (SPIE) Conference Series, High spatial resolution and high contrast optical speckle imaging with FASTCAM at the ORM*
- Labeyrie A., 1970, *A&A*, 6, 85
- Lacour S., Tuthill P., Amico P., Ireland M., Ehrenreich D., Huelamo N., Lagrange A.-M., 2011, *A&A*, 532, A72
- Lohmann A. W., Weigelt G., Wirtzner B., 1983, *Appl. Opt.*, 22, 4028
- Meyer L., Ghez A. M., Schödel R., Yelda S., Boehle A., Lu J. R., Do T., Morris M. R., Becklin E. E., Matthews K., 2012, *Science*, 338, 84
- Neichel B., Rigaut F., Bec M., Boccas M., Daruich F., D’Orgeville C., Fesquet V., Galvez R., Garcia-Rissmann A., Gausachs G., Lombini M., Perez G., Tranco G., Upadhy V., Vucina T., 2010, in *Society of Photo-Optical Instrumentation Engineers (SPIE) Conference Series Vol. 7736 of Society of Photo-Optical Instrumentation Engineers (SPIE) Conference Series, The Gemini MCAO System GeMS: nearing the end of a lab-story*
- Petr M. G., Coude Du Foresto V., Beckwith S. V. W., Richichi A., McCaughrean M. J., 1998, *ApJ*, 500, 825
- Primot J., Rousset G., Fontanella J. C., 1990, *Journal of the Optical Society of America A*, 7, 1598
- Rengaswamy S., Girard J. H., Montagnier G., 2010, in *Society of Photo-Optical Instrumentation Engineers (SPIE) Conference Series Vol. 7734 of Society of Photo-Optical Instrumentation Engineers (SPIE) Conference Series, Speckle imaging with the SOAR and the very large telescopes*
- Rigaut F. J., Ellerbroek B. L., Flicker R., 2000, in P. L. Wizinowich ed., *Society of Photo-Optical Instrumentation Engineers (SPIE) Conference Series Vol. 4007 of Society of Photo-Optical Instrumentation Engineers (SPIE) Conference Series, Principles, limitations, and performance of multiconjugate adaptive optics*. pp 1022–1031
- Schödel R., 2010, *A&A*, 509, A260000+
- Schödel R., Merritt D., Eckart A., 2009, *A&A*, 502, 91
- Schödel R., Morris M. R., Muzic K., Alberdi A., Meyer L., Eckart A., Gezari D. Y., 2011, *A&A*, 532, A83+
- Schödel R., Najarro F., Muzic K., Eckart A., 2010, *A&A*, 511, A18+
- Stetson P. B., 1987, *PASP*, 99, 191
- Tuthill P., Lloyd J., Ireland M., Martinache F., Monnier J., Woodruff H., ten Brummelaar T., Turner N., Townes C., 2006, in *Society of Photo-Optical Instrumentation Engineers (SPIE) Conference Series Vol. 6272 of Society of Photo-Optical Instrumentation Engineers (SPIE) Conference Series, Sparse-aperture adaptive optics*
- Wang Q. D., Dong H., Cotera A., Stolovy S., Morris M., Lang C. C., Munro M. P., Schneider G., Calzetti D., 2010, *MNRAS*, 402, 895
- Weigelt G., Beuther H., Hofmann K., Meyer M. R., Preibisch T., Schertl D., Smith M. D., Young E. T., 2006, *A&A*, 447, 655
- Weigelt G. P., 1977, *Optics Communications*, 21, 55

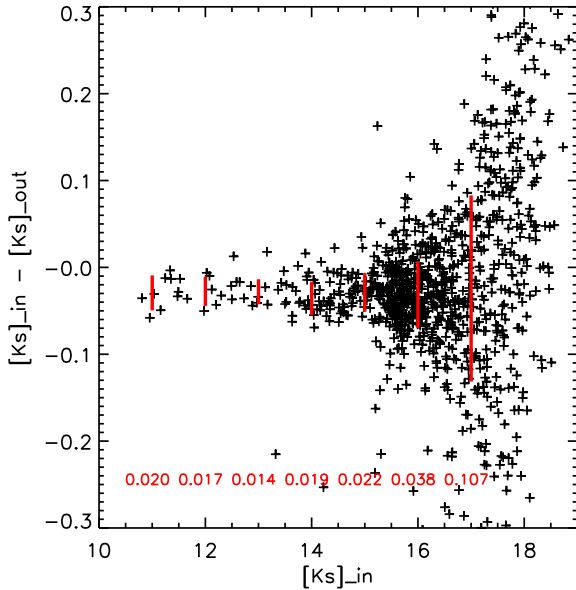


**Figure A1.** Plot of the difference between input and output  $Ks$ -magnitudes vs. input magnitudes for the simulation described in section A1.

## APPENDIX A: PHOTOMETRY AND ASTROMETRY ON IMAGES RECONSTRUCTED VIA HOLOGRAPHY

The primary use of holographic imaging may be high precision astrometry and photometry. We therefore dedicate this appendix to a more detailed analysis of some of the main sources of uncertainties. Also, this appendix serves to show that holography does not (or hardly) suffer from some of the typical problems of standard deconvolution procedures, like for example cross-correlations between pixels, ringing, or the creation of spurious sources. We introduce a new method for estimating the uncertainties of pixel values in images that can be of general interest, not just for holography.

### A1 Systematic effects

We produced simulated data in order to test whether holography may lead to a systematic bias in photometry or astrometry. As input for the simulation we took the stellar positions and fluxes measured in a NaCo/VLT image of the Galactic centre from 28 May 2008. The data are described in the last line of Table 1 in Schödel et al. (2009). The speckle PSFs were simulated with the speckle simulator of Rengaswamy et al. (2010), assuming  $0.8''$  seeing in the visual, a wind speed of  $10 \text{ m s}^{-1}$ , an airmass of 1.2, and an exposure time of 0.15 s. The gain and readout noise of NaCo's detector were used. Readout and photon noise were added to the 4000 artificial speckle frames. After holographic reconstruction PSF fitting photometry and astrometry was performed with *StarFinder*. Figure A1 shows a plot of the difference between the input and output magnitude vs. the input magnitude for each star. There is a small systematic difference of about 0.03 mag. This shift is due to the uncertainty of the zero point, which is caused by the exact choice

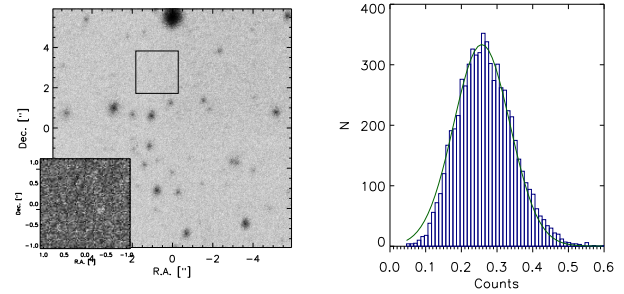


**Figure A2.** Left: Noise map for the reconstructed  $Ks$ -band image of the GC. The inset shows a zoom into a region of the noise map devoid of bright stars. Right: Histogram of pixel values in top right image, with Gaussian fit over-plotted.

of the parameters for PSF extraction (mainly the size of circular mask applied to the PSF). But there is no apparent trend and the scatter is small at all magnitudes. Hence, from the simulations there is no evidence for any systematic photometric or astrometric errors that could be introduced by the holographic technique.

### A2 Noise properties

Holographic image reconstruction can be considered a deconvolution technique. As is well known, deconvolution can introduce artifacts into images, like the typical ringing around stars in the Wiener deconvolution or the grainy background and photometric bias on faint sources in the case of the Lucy-Richardson algorithm. Deconvolution can alter the noise statistics by introducing covariances between the pixel (the mentioned effects are discussed, e.g., in Schödel 2010). The absence of any significant covariances between pixels is fundamental for the application of PSF fitting photometry and astrometry programs, like DAOPHOT (Stetson 1987) or *StarFinder* (Diolaiti et al. 2000).

Fortunately, speckle holography is a linear algorithm and a large number of independent frames are averaged before division in Fourier space. While graininess of the background (covariances between pixels) can occur in images reconstructed from a small number of speckle frames, this effect rapidly disappears with an increasing quantity of data.

It is *a priori* not clear whether one can estimate the noise in images reconstructed with the holography method in the same way as in standard long-exposure images, where readout and photon noise usually dominate the noise statistics. It is not necessarily trivial, how the (unavoidable) errors made at estimating the instantaneous PSFs are translated into the final reconstructed image. Also, particularly at short integration times, additional sources of uncertainty may become important, like systematic errors in the applied flat-fields or errors introduced by correlated noise in the readout electronics (often visible in short-exposures, e.g., in the form of horizontal stripes). Furthermore, the signal-to-noise ratio in mosaicked images will generally not be constant across the image.

A simple and reliable way of creating noise maps that include basically all of those effects is through creating images from independent sub-sets of the data, so-called *sub-maps*. The noise at each pixel can then be estimated as the uncer-

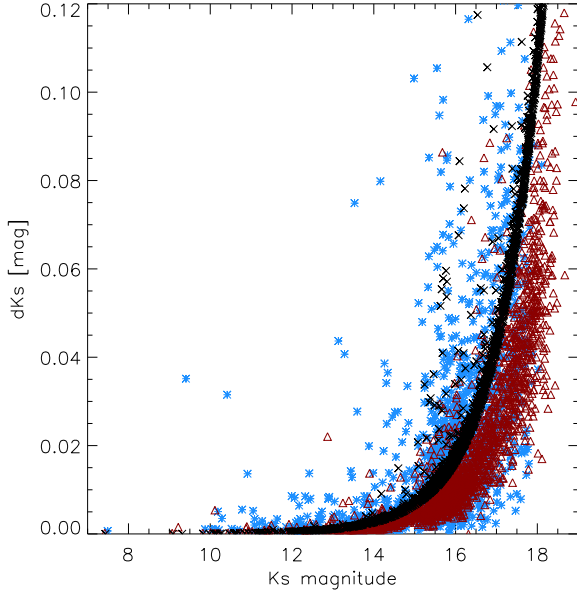


**Figure A3.** Photometry on the holographically reconstructed *Ks*-band image of the GC: Comparison of different methods to estimate the uncertainties. The black crosses, arranged in a line with very low scatter, represent the formal uncertainties estimated by *StarFinder*, using only Gaussian and photon noise estimated with *StarFinder* routines. The blue asterisks show uncertainty estimates from comparing the photometry obtained on images reconstructed from three separate sub-sets of the data. The red rectangles show the formal uncertainties computed by *StarFinder* when using a noise map derived from the images reconstructed from seven separate sub-sets of the data.

tainty of the mean of the sub-maps at a given pixel. As an example, in the left panel of Fig. A2, we show the noise map, estimated from 7 sub-maps, for the *Ks*-band image of the GC (Fig. 1, bottom panel). The inset shows the magnified view of a region devoid of bright stars. There appears to be no obvious cross-correlation between the pixels. The auto-correlation of this region shows no obvious structures, apart from a central peak at offset (0, 0). If the peak of the auto-correlation map is normalized to one, then all other values are  $\leq 5 \times 10^{-5}$ . The histogram of the pixel values in the inset is shown in the bottom left panel. The over-plotted fit shows that the pixel values follow closely a Gaussian distribution. We inferred from experiments with the data that Gaussian noise statistics can be obtained already with only several hundred frames.

### A3 Estimating uncertainties

For astrometry and photometry we used *StarFinder*, a PSF fitting program package, that was specifically developed for the analysis of AO images. Given a noise map for an image, *StarFinder* will calculate the formal uncertainties of the positions and fluxes of point sources. This noise map can be calculated from the relevant quantities, like read-out-noise, dark current, gain, number of exposures. Gaussian noise can also be estimated directly from the image with the help of the *StarFinder* routine GAUSS\_NOISE\_STD.

We explored three different methods to estimate photometric and astrometric uncertainties: (1) The *formal method*, in which uncertainties are evaluated by *StarFinder*, given a noise map composed only of Gaussian plus photon noise. The Gaussian noise was evaluated directly from the image with the GAUSS\_NOISE\_STD routine. (2) The *sub-map method*: Instead of using a noise map,  $N$  independent images are analysed. The uncertainties are estimated from the error of the mean of the stellar positions and fluxes. The independent images, termed *sub-maps*, are created from non-overlapping subsets of the data, with each set containing a fraction of  $1/N$  of all frames. (3) The *noise map method*: The sub-maps (see previous point) are used to create a noise map, in which each pixel is assigned the error of the mean at its location (i.e., standard deviation divided by  $\sqrt{N}$ ). This noise map is then input into *StarFinder*. Note that estimating the noise is itself a process that is subject to uncertainties. Therefore, for a small number of sub-maps, e.g.  $N = 3$ , the noise map may contain pixels that deviate significantly from the local mean noise. For small  $N$ , it can therefore be good practice to median-smooth the noise map, e.g., with a square box of 3 to 4 pixels width. Here, we use  $N = 7$  to create noise maps, with no smoothing.

A comparison of point source photometry with the three methods is shown in Fig. A3 ( $N = 3$  for the sub-map method and  $N = 7$  for the noise map method). There is very good general agreement between the three methods. It therefore appears that a holographically reconstructed image can be analysed with PSF fitting software in the same way as standard long-exposures or AO images. The formal method shows hardly any scattering of the uncertainties and very few outliers. This indicates that the true uncertainties may be significantly under-estimated for some sources. As concerns the other two methods, visual inspection of the image revealed that stars with uncertainties significantly above the mean for a given magnitude, were located close to brighter companions. This agrees with our expectations. Note that the sub-map method with  $N = 3$  leads, as expected, to a larger scatter in the uncertainties and to a reduced sensitivity compared to the noise map method.

In contrast to the formal method, which tends to lead to the detection of numerous spurious sources in the halos of bright stars, both the sub-map and the noise-map methods lead to robust source detection, as long as adequate flux and point-source correlation thresholds are applied. The sub-map method has been applied previously to both speckle and AO data (Ghez et al. 2008). We consider the noise map method the most attractive technique because it combines robust point source detection with high sensitivity and realistic estimates of the uncertainties directly from the data, thus including a broad range of error sources (photons, readout, electronics, flat field etc.). Note that the noise map method is – to the best of our knowledge – a simple yet new method that can be attractive for a broad range of astronomical images, not only for holographically reconstructed ones. For example, the noise map method can also be applied to AO images and may serve to estimate the uncertainties in deconvolved images, too.

### A4 Spatial and temporal stability of the PSF

*StarFinder* assumes a perfectly known and spatially stable



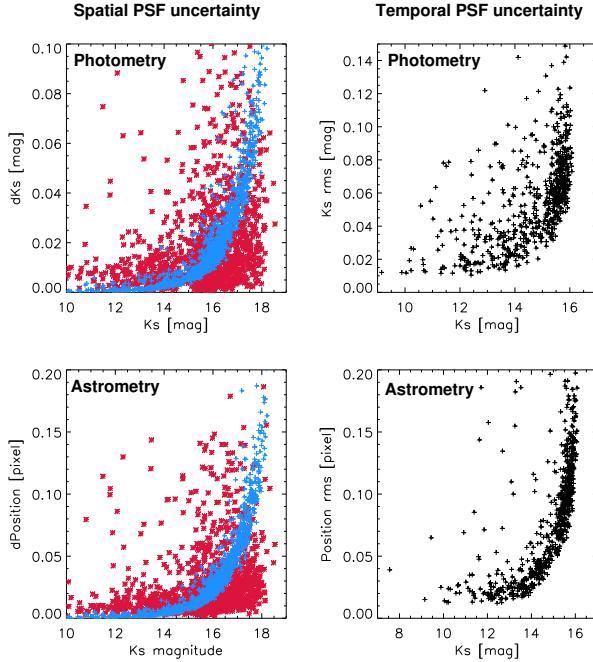


**Figure A4.** Top left: Photometric uncertainties caused by spatial variations of the PSF in the holographic  $Ks$ -band image of the GC. Blue crosses represent the statistical uncertainties, red asterisks show the uncertainties caused by the spatial variability of the PSF. Top right: Photometric uncertainties caused by temporal variations of the PSF for the same data. Bottom left and right: As top left and right, but for astrometric uncertainties.

PSF, which is, of course, an assumption that will always be violated to a certain degree, mainly because of anisoplanatic effects. We examined this problem on the GC  $Ks$ -band image (section 3). We performed repeated PSF fitting photometry and astrometry with three different PSFs, estimated from independent sets of reference stars. Note that mean offsets in photometry and astrometry will appear when an image is analyzed with slightly different PSFs. Those mean offsets (on the order of 0.02 – 0.03 mag for photometry and 0.001 – 0.01 pixels in each axis for astrometry) are not relevant for our analysis and were removed before combining the lists resulting from the different runs of *StarFinder*. Subsequently, uncertainties were estimated from the standard deviation of the measurements with the three different PSFs. The photometric uncertainties are shown in the left panel of Fig. A4. As expected, the PSF uncertainties appear to be independent of stellar magnitude and are small, with a median of 0.008 magnitudes. The astrometric uncertainty, shown in the right panel of Fig. A4, has a median uncertainty of  $< 0.01$  pixels in each axis. Note that PSF uncertainties are the dominating source of uncertainty for sources of  $Ks \leq 15$ .

The photometric and astrometric uncertainties from the *temporal* fluctuation of the PSF were estimated by running *StarFinder* on images reconstructed from 25 consecutive data cubes of  $\sim 500$  frames each (GC  $Ks$ -band data). The uncertainties caused by temporal fluctuations of the PSF were estimated from the standard deviation of the measurements on the 25 different images, after correction of the mean offsets (which were somewhat smaller than for the

spatial PSF variation). They are shown in the right panel of Fig. A4 and dominate the uncertainties for bright stars. They are  $\leq 0.02$  mag for stars brighter than  $Ks \approx 14$ . The corresponding astrometric uncertainties are  $\leq 0.03$  pixel in each axis for stars brighter than  $Ks \approx 14$ .

We conclude that holographic imaging can lead to images with a spatially and temporally stable PSF. The photometric uncertainty - using the noise map method preferred by us - is  $\leq 0.01$  mag for  $Ks \leq 15$  stars. The  $3\sigma$  detection limit in the holographically reconstructed image of the GC is  $Ks \approx 19$ , for a total integration time of 1875 s.

## APPENDIX B: $K$ -BAND IMAGING OF THE GALACTIC CENTRE WITH KECK/NIRC

Between 1995 and 2005 the Galactic centre was observed with the speckle camera NIRC at the Keck telescope in order to monitor the motions of stars around Sgr A\* (e.g. Ghez et al. 2008). We have applied our holographic image reconstruction method to these data. They are of special interest because the holographic technique allows us to detect fainter sources than in the previously used SSA images. Thus, it becomes possible to track the orbital motion of stars that are too faint to have been picked up in the previously used SSA images. Also, crowding can lead to systematic errors in the measured positions of the stars close to Sgr A\* (see Ghez et al. 2008; Gillessen et al. 2009). The excellent Strehl ratio of the holographic images enables us to better disentangle close sources than in previous analyses of these data. Since the methodology presented in this paper was in large part developed and fine-tuned with NIRC speckle data of the GC and since the holographically reconstructed NIRC/Keck GC data have been used in recent work (Meyer et al. 2012) and will be used in future publications, this work is the natural place to explain the corresponding details.

As an example, we present a data set from April 2005. About 10,000 speckle frames with an exposure time of 0.1 s were used for image reconstruction. The stars IRS 16C, IRS 16NW, and IRS 16SW were used as point source references ( $Ks = 9.9$ ,  $Ks = 10.1$ , and  $Ks \approx 10.2$ , see Schödel et al. 2010).

A special feature of the NIRC GC speckle data is that they were collected in the so-called *stationary mode*, which keeps the pupil fixed on the detector. This avoids a variable contribution of the secondary spider to the diffraction patterns. A part of the FOV was masked in all NIRC data, with the mask changing relative to the stars because of the sky rotation. In order to deal with the variable FOV, we constructed a weight map to adjust the final reconstructed image. The weight map was created by running the corresponding masks of all the speckle frames through the same holographic reduction pipeline. We used an Airy PSF for a circular 10m-aperture for apodisation of the final image. The FWHM of this Airy function,  $\sim 0.05''$ , corresponds to the angular size of a resolution element of the Keck telescopes in the  $K$ -band.

In Fig. B1 we show close-ups on the environment of Sgr A\* from an SSA and a holography image for the April 2005 data, as well as from a laser guide star assisted AO image from July 2005 (Ghez et al. 2008). A plot of photometric

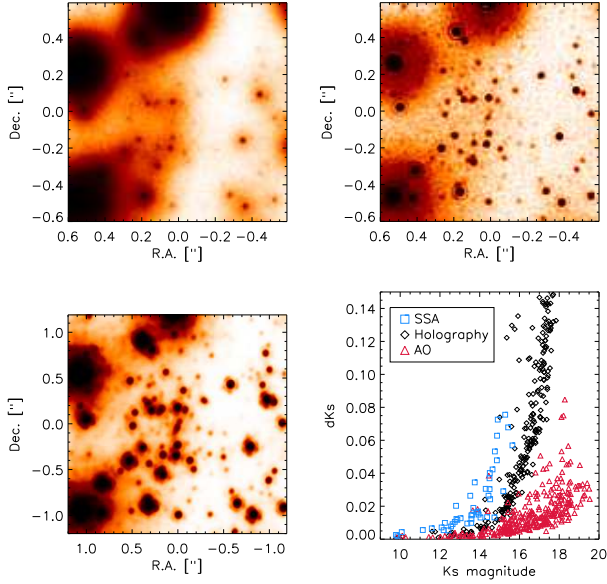


**Figure B1.** Speckle holography of the Galactic centre with NIRC/Keck. Upper left: SSA image of the central arcseconds of the Galactic centre from April 2005. Upper right: Image reconstructed with the holography technique. Lower left: NIRC2/Keck LGS AO image of the Galactic centre from July 2005. Lower right: Photometric uncertainty vs.  $K$ -magnitude for sources detected within  $2''$  of Sgr A\*: blue squares: SSA; black diamonds: holography; red triangles: AO. The detection threshold was set to  $5\sigma$ .

uncertainty vs. magnitude for the point sources detected in the three images is shown in the same Figure. Lucky imaging was applied to the SSA reconstruction, with selection of the best 10% of the frames. The exposure times of the AO ( $\sim 900$  s) and holography ( $\sim 1000$  s) images are comparable. As can be seen in Fig. B1, holographic image reconstruction provides excellent spatial resolution with a very well calibrated PSF in the reconstructed image. The Strehl is about 40%. As shown in the bottom right panel of Fig. B1, the holography image is roughly 2 mag deeper than the SSA image, while the AO image is about 2 mag deeper than the holography image.